Mixing Times in a Turbulent Stirred Tank by Means of LES

H. Hartmann, J. J. Derksen, and H. E. A. van den Akker
Kramers Laboratorium voor Fysische Technologie, Delft University of Technology, Prins Bernhardlaan 6, 2628 BW, Delft, The Netherlands

DOI 10.1002/aic.10997
Published online September 26, 2006 in Wiley InterScience (www.interscience.wiley.com).

In turbulent liquid mixing, the performance of a stirred tank is usually expressed as the time it takes to homogenize a passive scalar concentration starting from a segregated state. Numerical prediction of mixing times requires solving the flow field and the associated passive scalar. A novel numerical approach is presented to passive scalar mixing in an agitated tank. In addition to a large-eddy simulation based on lattice-Boltzmann discretization of the Navier-Stokes equations, the convection-diffusion equation governing passive scalar transport has been solved by finite volume discretization. Numerical diffusion has been effectively eliminated by applying a TVD scheme. With this hybrid approach we study mixing in a Rushton turbine stirred vessel at Re = 24,000. The simulations were designed such that their results can be critically assessed with experimental data. The simulations are in (at least) qualitative agreement with the experiments, and allow for assessment of how mixing times defined in various ways relate. Also the role of the impeller size has been investigated. The numerical method needs improvement in the sense that it is not exactly mass conservative, which likely is due to the fixed-grid approach in combination with a non-fixed (revolving) impeller. © 2006 American Institute of Chemical Engineers *AIChE J,* 52: 3696–3706, 2006
Keywords: stirred tank, turbulence, mixing time, LES, scalar transport

Introduction

Experimental research on turbulent scalar mixing

Stirred tanks play an important role in the chemical, pharmaceutical, food and water treatment industries. The quality of paints, polymers, detergents, drugs and foodstuffs depends on the layout and operating conditions of the stirred tank. As a result, the mixing performance is of crucial importance to achieve process optimization.

Much experimental research effort has been devoted to describing and understanding the velocity characteristics of turbulent stirred tank flow (for example, Yianneskis et al., 1987; Schäfer et al., 1998), together with the power required to drive the stirrer (Rushton et al., 1950; Holmes et al., 1964). The essential requirement of mixers in liquid systems is, however, to bring together two or more fluids which are initially separate. This implies the need for information of the scalar mixing characteristics of the flow systems.

A global characterization of passive scalar mixing is the mixing time. Roughly speaking, it is the time to achieve complete (that is, over the whole vessel) homogenisation of an inserted passive scalar. A large number of experimental studies has focused on mixing performance in terms of the mixing time for different tank, impeller, and injection configurations. Kramers et al. (1953) were among the first to report on mixing time in a propeller agitated tank as a function of the baffle position and impeller rotational speed. Moo-Young et al. (1972) investigated the influence of Newtonian and non-Newtonian fluids in different-flow configurations. Others have focused on the impeller configurations and/or operating conditions in transitional and turbulent flow regions (Hoogendoorn and Den Hartog, 1967; Shiue and Wong, 1984; Sano and Usui, 1985; Bouw-

Correspondence concerning this article should be addressed to H. Hartmann at Hugo.Hartmann@WLdelft.nl.

mans et al., 1997; Distelhoff et al., 1997). Results of several studies have been combined to empirical correlations, which are of use for industrial applications (Prochazka and Landau, 1961; Sano and Usui, 1985; Ruszkowski, 1994).

In literature, there is no standardization of a mixing time experiment. The passive tracer is injected at various injection speeds, thereby, influencing the relative importance of jet mixing and stirred mixing. The position of the injection point and the number and position of monitor points are additional variables that are not standardized. Finally, the definition of what is considered homogeneous varies from study to study. Most of the studies report the mixing time based on a concentration % (for example, Bouwmans et al. (1997) and Distelhoff et al. (1997)), others determine mixing time by the variance of concentration fluctuations (for example, Ruszkowski (1994)). As a result, measured mixing times and mixing time correlations should be viewed with great care. This is specifically important when one wants to compare simulation results with experimentally obtained mixing times. In executing and post-processing the simulations, the experimental procedures (if known) should be mimicked as closely as possible.

Potential of CFD on scalar mixing

First and foremost, numerical predictions of scalar mixing require a realistic representation of the flow field, including its turbulent characteristics. Simulations based on the Reynolds-averaged Navier-Stokes (RANS) equations (contained in various commercial software packages) provide a reasonably accurate picture of the time-averaged flow field in the tank as a whole. However, they invariably underpredict the turbulent kinetic energy (that is, the fluctuation levels) in the impeller discharge stream by about 50% (for example, Hartmann et al., 2004b). This will certainly affect the predictions of the mixing patterns and mixing time in stirred tanks.

Osman and Varley (1999), Jaworski et al. (2000) and Bujalski et al. (2002) have reported mixing time predictions, based on the RANS approach within a sliding mesh or multiple frames of reference (MFR) framework. The sliding mesh method is fully transient, while the MFR method provides a steady-state approximation. With the same grid, the sliding mesh approach is considered more accurate, but it is also much more time-consuming compared to MFR. In spite of the use of the sliding mesh approach, the predicted mixing times were found, in general, 2–3 times higher than the measured values (for example, Osman and Varley, 1999; Jaworski et al., 2000; Bujalski et al., 2002), which is understandable with the underprediction of the turbulence levels in mind.

Large-eddy simulations (LES) are better capable of resolving the turbulent nature of the flow. In LES the flow is resolved down to the level of the computational grid, that there is a clear distinction between resolved and unresolved scales. If the grid is sufficiently fine, the modeling of unresolved scales is less complicated and speculative than RANS closure modeling, leading to better predictions of (among other applications) stirred-tank flow (Eggels, 1996; Derksen and Van den Akker, 1999; Hartmann et al., 2004b, a; Yeoh et al., 2004; Bakker and Oshinowo, 2004). The LES methodology has been recently applied for a mixing time simulation in the study reported by Yeoh et al. (2005). Their simulation was designed to match the experimental setup of Lee (1995).

In earlier work (Derksen and Van den Akker, 1999; Hartmann et al., 2004b, a) we have demonstrated that using lattice-Boltzmann (LB) discretization of the Navier-Stokes equations is highly beneficial for performing LES: the (parallel) computational efficiency (not hampered by the complexity of the shape of the flow domain) allows for fine grids with still reasonable run times. To solve passive scalar transport in the LB-generated flow field we make use of a finite volume (FV) technique. We do not use the LB method for this for two main reasons, (1) It requires more computer memory (in fact solving the convection diffusion equation for the scalar would require as much memory as solving the Navier-Stokes equation for the fluid flow), and (2) In finite volumes schemes, well-established techniques are available to suppress numerical diffusion. In this work we apply second-order TVD interpolation. We use explicit time-stepping, which maintains the parallel efficiency of the simulations.

A fixed grid is used in our LB code; the (moving) parts of the geometry (for example, the revolving impeller, the stationary baffles) are represented through an immersed boundary method. For representing moving walls in the scalar field, a method (termed ghost-cell method here) has been developed that imposes zero-normal-gradient boundary conditions at (static and moving) solid walls at approximately the same (off-grid) locations as the immersed boundary method for imposing the no-slip conditions for the fluid flow.

In this article the methodology briefly sketched earlier will be detailed, and critically evaluated. The results of the simulations comprise full scalar fields evolving in time. This information allows for assessing the sensitivity of the mixing time with respect to its definition. The starting point is a numerical representation of the mixing time experiment of Distelhoff et al. (1997). Furthermore the scaling of the mixing time with impeller size has been investigated.

Flow system

The stirred tank used in this work was a standard configuration cylindrical tank of dia. $T = 147$ mm, with four equispaced baffles of width $0.1T$ mounted along the perimeter of the tank (Distelhoff et al., 1997). The liquid height was set equal to the tank dia., $H = T$. The impeller was a six-bladed Rushton turbine with standard dimensions, mounted at height $T/3$. A schematic representation of the flow system is shown in Figure 1. The flow system can be fully characterized by the flow Reynolds number ($\mathrm{Re} = ND^2/\nu$) if geometric similarity is maintained. With an impeller speed (N) of 10 s^{-1}, $D = T/3$, and a kinematic viscosity of $1.0 \cdot 10^{-6}$ m^2/s (tap water at room temperature) the Reynolds number yields 24,000 (as also used in Distelhoff et al., 1997). Next to $D = T/3$, also cases with $D = T/4$, and $D = T/2$ have been considered.

Simulation Procedure

Large eddy simulation

For the simulation of flow at industrially relevant Reynolds numbers (that is, at strongly turbulent conditions), direct simulation of the flow is not feasible and turbulence modeling is required. In an LES, the small scales in the flow are assumed to be universal and isotropic, and the effect the small scales have on the larger scales is modeled with a subgrid-scale (SGS)

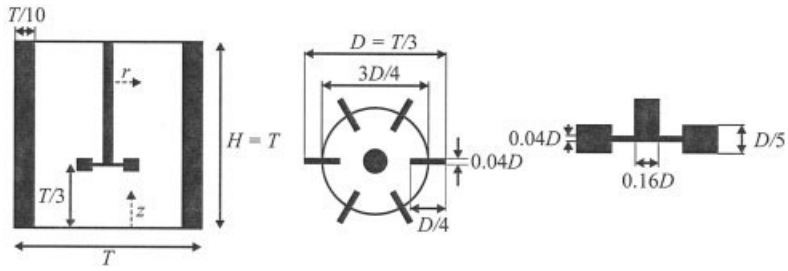

Figure 1. Rushton turbine stirred tank.

Cross-section of the tank (left). Plan view and cross-section of the impeller (right). At the top level there is a lid. The impeller is a Rushton turbine mounted at height $T/3$ and has a dia. $T/3$. In the simulations presented in this work, impeller sizes of $T/4$ and $T/2$ have been used as well.

model. The filtering of the small-scale motion is based on the assumption that the motion of the smallest scales is isotropic in nature and that the subgrid-scale energy is dissipated via an inertial subrange that has a geometry independent character. The SGS model applied in this research is a standard Smagorinsky model (Smagorinsky, 1963). For more details on the LES methodology used we refer to Hartmann et al. (2004b, a) and Derksen and Van den Akker (1999). A lattice-Boltzmann method (Chen and Doolen, 1998) was used for solving the filtered momentum equations. The specific scheme we used was introduced by Somers (1993). The entire tank was simulated on a uniform, cubic computational grid. Inside the computational domain, the noslip boundary conditions at the cylindrical tank wall, the baffles, the impeller, and the impeller shaft were imposed by an immersed boundary technique (termed adaptive force-field technique in (Derksen and Van den Akker, 1999)).

Scalar transport

In order to describe scalar transport, the convection-diffusion equation needs to be solved. Eggels and Somers (1995) have performed scalar transport calculations on free convective cavity flow with the lattice-Boltzmann discretization scheme. This scheme is more memory intensive than a finite volume formulation of the convection-diffusion equation. In a finite volume discretization we only need to store two or three (depending on the time integrator; Euler-forward or Adams-Bashford, respectively) double precision values per grid node, whereas the lattice-Boltzmann discretization typically requires 18 single-precision variables per grid node.

The convection-diffusion equation in compressible form reads

$$\frac{\partial \rho\phi}{\partial t} + \frac{\partial u_j \rho\phi}{\partial x_j} = \frac{\partial}{\partial x_j}\left(\rho\Gamma \frac{\partial \phi}{\partial x_j}\right) + S_\phi \tag{1}$$

with ρ the density of the continuous phase, ϕ a general scalar, u_j the resolved velocity (component j), Γ the diffusion coefficient, and S_ϕ a source term. The effect of the unresolved fluid motion on the transport of the scalar is represented through an eddy diffusivity Γ_e.

The diffusion coefficient Γ in Eq. 1 is the sum of the molecular diffusion, and eddy diffusion $\Gamma = \Gamma_{mol} + \Gamma_e$. The eddy diffusivity is taken proportional to the eddy viscosity emerging from the Smagorinsky subgrid-scale model; the proportionality constant being the inverse turbulent Schmidt number $\mathrm{Sc}_t = \nu_e/\Gamma_e$. We take $\mathrm{Sc}_t = 0.7$. The reason it is taken smaller than one is that in liquid systems with molecular Schmidt numbers of the order of 10^3, the scalar spectrum contains higher frequencies than the dynamic spectrum, and, therefore, subgrid-scale scalar eddy diffusion is stronger than momentum diffusion due to subgrid-scale eddies. We expect the simulation results to be hardly sensitive to the choice of Sc_t: subgrid-scale fluid motion is at least one-order of magnitude weaker than resolved fluid motion (Derksen, 2003). The latter will dominate the evolution of the scalar concentration field.

Since the LB scheme is a compressible scheme, we have implemented the discretized form of the compressible convection-diffusion equation. In this context it should be noted that the maximum velocity (which is approximately the tip speed) is set sufficiently low (approximately 0.1 in LB units) for meeting the incompressibility limit in the lattice-Boltzmann scheme.

For reasons of simplicity, we consider in the following discussion on the discretization of the convection diffusion equation the one-dimensional (1-D) version of Eq. 1. Extension to multiple dimensions is straightforward. Integration over a finite volume ΔV, and over time Δt, and using the Gauss theorem leads to

$$\frac{\Delta V}{\Delta t}\left((\rho_i\phi_i)^{n+1} - (\rho_i\phi_i)^n\right) = (F_C\phi)^n_{i+(1/2)} - (F_C\phi)^n_{i-(1/2)} - (F_D)^n_{i+(1/2)}(\phi^n_{i+1} - \phi^n_i) + (F_D)^n_{i-(1/2)}(\phi^n_i - \phi^n_{i-1}) \tag{2}$$

where F_C and F_D are convective and diffusive prefactors, for example

$$F_{C;i+(1/2)} = (\rho u A)_{i+(1/2)} \tag{3}$$

and

$$F_{D;i+(1/2)} = \left(\frac{A\rho\Gamma}{\Delta}\right)_{i+(1/2)} \tag{4}$$

where u is the normal (resolved) velocity through the cell face with surface A.

The density, normal velocity components and the diffusion coefficient at the cell faces are approximated by linear inter-

polation between the surrounding cell nodes values. For reasons of simplicity, the time discretization in Eq. 2 is first-order Euler forward. We have implemented a second order accurate Adams-Bashford time discretization scheme.

The convection-diffusion equation is solved on the LES grid, and the time step is the same as the LES time step. The finite volume formulation presented is fully explicit; the update of the scalar value at cell node i, and time instant n is determined by the scalar values, velocity components and density at cell node i, and its surrounding nodes at time instant $n - 1$. An explicit scheme has restrictions on the time step in order to guarantee stability. However, the time step used for the LES is very small, and no stability problems were encountered in the scalar transport calculations.

The cell face values of the general scalar ϕ, needed for the convection terms (the first two terms on the right hand side of Eq. 2), have been approximated with a second-order TVD (total variation diminishing) scheme, that has been introduced by Harten (1983). This scheme belongs to the family of high-resolution schemes and does not suffer from numerical diffusion (in contrast to first order upwind, power-law and hybrid schemes (Patankar, 1980)), and it is unconditionally stable (contrary to central differences and QUICK (Leonard, 1979)). Following Roe (1981), the face value $\phi_{i+(1/2)}$ is written as the sum of a diffusive first-order upwind term and an antidiffusive one

$$\phi_{i+(1/2)} = \phi_i + \frac{1}{2}\Psi(r_{i+(1/2)})(\phi_{i+1} - \phi_i) \tag{5}$$

The antidiffusive part is multiplied by the flux limiter function $\Psi(r)$, which is a nonlinear function of r. The factor r is the upwind ratio of consecutive gradients of the solution and reads

$$r_{i+(1/2)} = \frac{\phi_{i+1} - \phi_i}{\phi_i - \phi_{i-1}} \tag{6}$$

According to Wang and Hutter (2001), the so-called superbee flux limiter is the least diffusive of all acceptable limiters. Therefore, we have used the superbee limiter throughout our simulations. The superbee limiter is defined as:

$$\Psi(r) = \max[0, \min[1, 2r], \min[r, 2]] \tag{7}$$

Ghost cell technique for scalar boundary conditions

The Neumann boundary condition at the non-square or moving (off-grid) objects in the flow domain are imposed by means of a newly developed method, which is applicable in the explicit formulation of the finite volume scheme. With our novel technique, the offgrid walls are more accurately represented (especially the impeller walls) compared to approximating the walls by stair step shapes. The algorithm makes use of ghost cells (that is, boundary cells with their cell centers outside the flow domain) in order to impose a zeronormal-gradient scalar constraint (that is, Neumann boundary condition) at the walls.

The scalar update is executed only for the cells with their centers inside the flow domain. In order to update the scalar in a cell near a wall, the scalar value in the neighbouring ghost cell is needed. The procedure for the determination of the scalar ghost cell value is shown in Figure 2. We consider a curved wall immersed in a Cartesian grid. Two scalar values on a line through the ghost cell center and perpendicular to the wall are estimated through bi-linear interpolation of the surrounding cell nodes. The spacing between the positions of the two estimated scalar values and the ghost cell center is taken equal to the lattice spacing. The scalar value at the ghost cell is determined via second order extrapolation with the two scalar values and the zero-normal-gradient constraint at the wall.

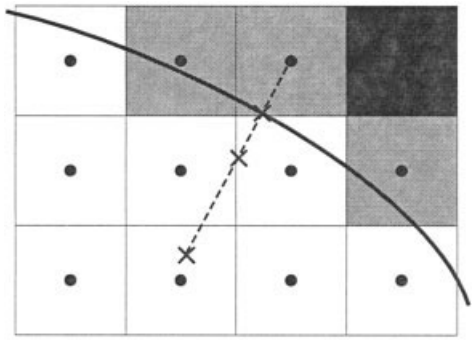

Figure 2. Determination of the scalar ghost cell value.

White cells are flow cells, grey cells are the ghost cells, black cells are exterior cells.

The ghost cell method is unconditionally stable, which is desirable in the explicit finite volume formulation. Other techniques that make use of body-fitted cells (socalled cut cells, Tucker and Pan (1999); Calhoun and LeVeque (2000)) will fail, as the allowable time-step scales with the cell volume. A drawback of the proposed technique is that it does not automatically guarantee scalar mass conservation.

Setup of the simulations

Mixing time simulations have been performed in a Rushton turbine stirred tank. The experimental benchmark case studied, is based on Distelhoff et al. (1997). A key parameter dominating the mixing time is the impeller diameter according to the correlation proposed by Sano and Usui (1985), and Ruszkowski (1994). We have investigated the influence of the impeller diameter on the mixing time by means of three flow simulations, each with a different impeller diameter. The tank over impeller diameter ratios were $T/D = 2$, $T/D = 3$ and $T/D = 4$. The Reynolds number in each of the simulations was 24,000.

For the coupled LES/scalar mixing simulations, a cubic, Cartesian grid of 240^3 lattice cells was defined. The diameter of the tank equals 240 lattice spacings, and, hence, the spatial resolution equals $T/240$ which corresponds to 0.6125 mm in the experiment. The temporal resolution is limited by the lattice-Boltzmann method. In order to meet the incompressibility limit in the lattice-Boltzmann discretization scheme, the tip speed of the impeller was set to approximately 0.1 lattice spacings per timestep. As a result, the impeller speed is different for the three impeller types. For the $T/D = 2, 3, 4$ cases the impeller makes a full revolution in 3,600, 2,400 and 1,800 time steps, respectively.

The memory requirements of the simulation are proportional to the grid size, resulting in an executable of about 2 GByte.

Table 1. Numerical Setup

Case	T/D	Feed: r/T	Feed: z/T	Feed: θ	Feed: r_p/T
2A	2	0.17	1	0°	0.0238
2B	2	0.1875	0.483	0°	0.0125
2C	2	0.35	0.333	0°	0.0125
2D	2	0.475	0.8	320°	0.0125
3A	3	0.17	1	0°	0.0238
3B	3	0.125	0.467	0°	0.0125
3C	3	0.211	0.333	0°	0.0125
3D	3	0.475	0.8	320°	0.0125
4A	4	0.17	1	0°	0.0238
4B	4	0.09375	0.458	0°	0.0125
4C	4	0.225	0.333	0°	0.0125
4D	4	0.475	0.8	320°	0.0125

The parameters varied are the impeller diameter and the feed location. Please note that θ increases in the direction of the impeller rotation, and $\theta = 0°$ is a mid-way baffle plane. r_p is the feed pipe radius.

The simulations were performed on an in-house PC cluster with eight Athlon 1,800+ MHz processors using an MPI message passing tool for communication within the parallel code. To calculate one time step takes about 58 s wall-clock time, hence an impeller revolution takes 1–2 days.

The scalar was injected in a quasi-steady state flow. This state was reached after 10–40 impeller revolutions (depending on the impeller size) starting from rest. Steady-state was checked by monitoring the total kinetic energy of the flow as a function of time.

Next to the impeller size, the injection position of the passive scalar has been varied. Four injection positions have been chosen, and as a result, four scalar mixing calculations have been performed simultaneously per flow simulation. An overview of the different cases is given in Table 1. Please note that θ increases in the direction of the impeller rotation.

Case 3A resembles the Distelhoff et al. (1997) experiment. The feed position is located at the top of the tank in a mid-way baffle plane (that is, $\theta = 0°$) at $0.17T$ from the tank centerline. Cases 2A and 4A have the same feed location and dimension of the feed pipe, but with tank over impeller ratio's $T/D = 2$ and $T/D = 4$, respectively.

Cases 2B, 3B and 4B have the feed pipe location at $0.1T$ above the top of the impeller blade, and at a radial position halfway the impeller blade. Cases 2C, 3C and 4C have the feed pipe located at disk height at $0.1T$ from the impeller tip. In cases 2D, 3D and 4D the passive scalar is injected in the wake of a baffle (that is, at 5° angle with respect to the baffle) at $0.8T$ axial height.

In all of our simulations the injection time was set to half an impeller revolution (that is, $Nt = 0.5$). This agrees with the tracer injection times in the experiments being less than 1% of a typical mixing time (Distelhoff et al., 1997).

Time traces of the scalar concentration were recorded at various monitoring points positioned in accordance with Distelhoff et al. (1997). A total of 32 monitoring points were set in the four vertical planes mid-way between two baffles. The points were located at $0.19T$, and $0.67T$ axial heights at $r/T = 0.126, 0.252, 0.361, 0.469$, respectively.

Results

Snapshots of the scalar concentration field

Figure 3 gives an impression of the scalar mixing process in the Rushton turbine stirred tank (Case 3A; $T/D = 3$) during the course of the simulation. In the first stage of the mixing process, high-concentration, macroscopic structures are identified that are advected by the flow from the tracer injection point (at the top of the tank) toward the impeller region. Such structures resemble those observed in visualization experiments in stirred-tank flow (such as the planar laser induced fluorescence (PLIF) experiments of Houcine et al. (1994). These structures are vigorously mixed once they hit the turbulence generated by the revolving impeller. After about 30 impeller revolutions, the scalar concentration is heading toward a homogeneous distribution.

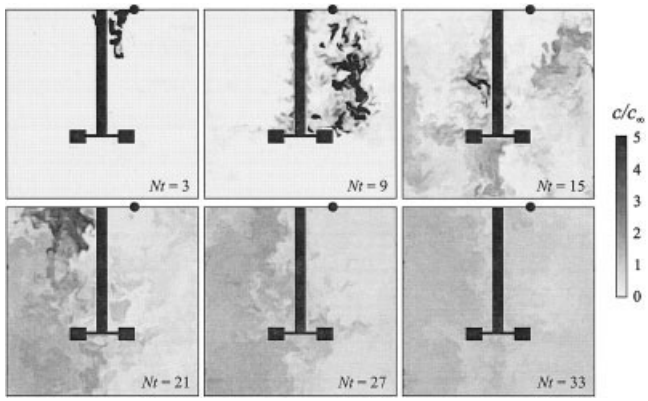

Figure 3. Case 3A (T/D = 3): instantaneous realizations of the scalar field in a mid-way baffle plane.

The scalar is injected at the top of the tank (black dot in the graphs).

The impact of the impeller diameter on the duration of the mixing process is illustrated in Figure 4. In this case, the passive scalar is injected 0.1T above the impeller disk. Again,

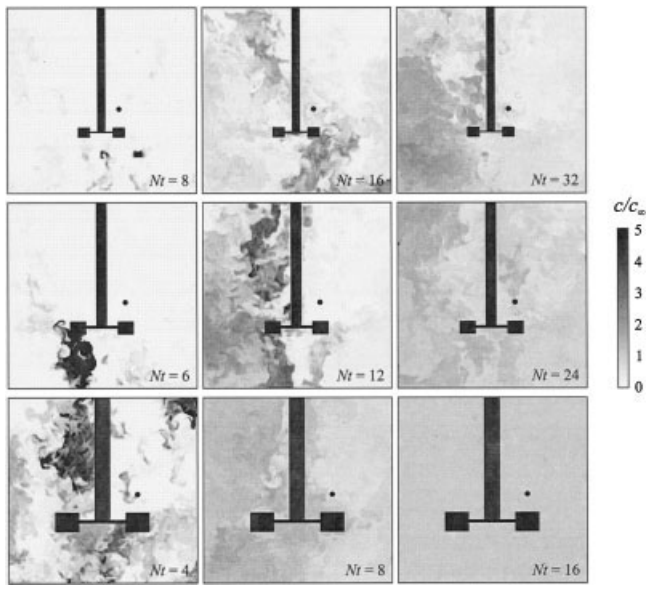

Figure 4. Instantaneous realizations of the scalar field (Cases 4B (T/D = 4), 3B (T/D = 3), 2B (T/D = 2) in upper, middle and lower graphs, respectively) in a mid-way baffle plane.

The scalar is injected $0.1T$ above the impeller (black dot in the graphs).

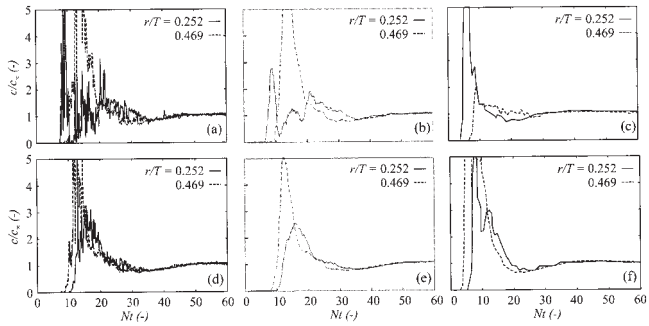

Figure 5. Case 3A (T/D = 3): simulated (a,d), filtered simulated (b,e) and experimental (c,f) time series at four monitoring points in a mid-way baffle plane ($\theta = 90°$).

The time series shown in Figures (a–c) are at axial position $z/T = 0.67$ and those in Figures (d–f) are at axial position $z/T = 0.19$.

high-concentration macroscopic structures are identified in all cases presented. The impeller diameter significantly influences the mixing process: the mixing time decreases at increasing impeller diameter. While in case 4B ($T/D = 4$) more than 32 revolutions are needed to reach a more or less homogeneous-scalar distribution, in case 2B ($T/D = 2$) only 8 revolutions are necessary to reach a similar situation.

Time series

In Figure 5 we compare simulated and experimentally measured time series of case 3A at four monitoring points (that is, two radial positions and two-axial heights) in a vertical midway baffle plane at $\theta = 90°$. We show two sets of simulated curves. One set with the full temporal resolution of the simulations (Figures 5a and 5d), and one set that has been filtered comparable to the filtering done in the experiments by Distelhoff et al. (1997) (Figures 5b and 5e). From a qualitative comparison between the simulated (Figure 5a,b,d and e), and experimentally measured (Figure 5c and f) time series it may be concluded that the time series compare well in terms of the path of the curves and the mixing timescale. The time-step used in the simulations is a factor of 20 smaller than the sampling time in the experiments. As a result, the simulated time-series show more concentration fluctuations compared to the experimentally measured time series.

The simulated time series at $z/T = 0.19$ show a delayed response on the tracer injection ($0 \leq Nt \leq 0.5$) compared to the time series at $z/T = 0.67$, which is to be expected as the tracer is injected at the top of the tank. The experimental time series show an earlier response on the tracer injection compared to the simulated time series. This could be due to momentum associated with the injection in the experiment. From the description in the experimental paper (Distelhoff et al., 1997) it is not clear what the momentum is associated with injecting the tracer dye. In the simulations, the tracer was added without adding any momentum.

Mixing time and coefficient of mixing

The mixing time θ_m, is the time required to mix the added passive tracer with the contents of the tank until a certain degree of uniformity is achieved. The precise definition of a certain degree of uniformity gives rise to confusion and ambiguity. If we determine it from a concentration time trace at one location in the tank, then ideally that location has to represent the state of mixing of the entire vessel. Distelhoff et al. (1997) measured mixing times where the concentration variations were smaller than 10%, 5% and 1% of the fully mixed concentration. These concentrations are called the 90%, 95% and 99% concentration. The mixing times defined by the 90% and 95% concentration varied by up to 27% and 21%, respectively, between different regions of the tank. These uncertainties can be reduced by averaging the measurements obtained simultaneously at several locations. The variation over the vessel between the mixing times for the 99% concentration was found substantially smaller. Based on these observations, Distelhoff et al. (1997) based their mixing time on the 99% concentration.

Another way of defining a degree of mixing is through the spatial variance of the concentration measured at various positions in the tank. In order to have a precise definition of mixing times, the coefficient of mixing is introduced. It is defined as

$$c_{mix} = \sqrt{\left(\frac{\Sigma_i \left(\frac{c_i - \bar{c}}{\bar{c}} \right)^2 \Delta V_i}{\Sigma_i \, \Delta V_i} \right)} \tag{8}$$

where index i stands for the location of the monitoring point with volume ΔV, and $i = 1, \ldots, K$, where K is the total number of monitoring points. The volume averaged mean concentration $\bar{c}$, is calculated as

$$\bar{c} = \frac{\Sigma_i \, (c_i \Delta V_i)}{\Sigma_i \, \Delta V_i} \tag{9}$$

The method provides the concentration variance of points in different regions of the tank. In order to relate the coefficient of mixing to a concentration % (for example, the 99% concentration) we have performed a numerical experiment that is explained in the appendix. The result is a linear relationship with a negative slope between c_{mix}, and the concentration %

$$c_{mix} = 0.17 \left(\frac{100 - c_{\%}}{30} \right) \tag{10}$$

where $c_{\%}$ is the concentration %.

The coefficient of mixing as a function of time calculated from the concentrations at the 32 monitoring points is shown in Figure 6, where all cases have been summarized in three graphs. In Figure 6a the data is missing for $Nt < 2$, due to a processing error. The three graphs show similarities. In the first stage of the mixing process, the macroscopic high-concentration structures are broken up and mixed into smaller structures with lower concentration. The coefficient of mixing strongly fluctuates with a value higher than one, and no clear trend is observed. In the second stage, all three graphs reveal an exponential decay of the coefficient of mixing. This has also been observed in Ruszkowski's experiments (Ruszkowski, 1994). In the final stage of the simulations, the coefficient of mixing

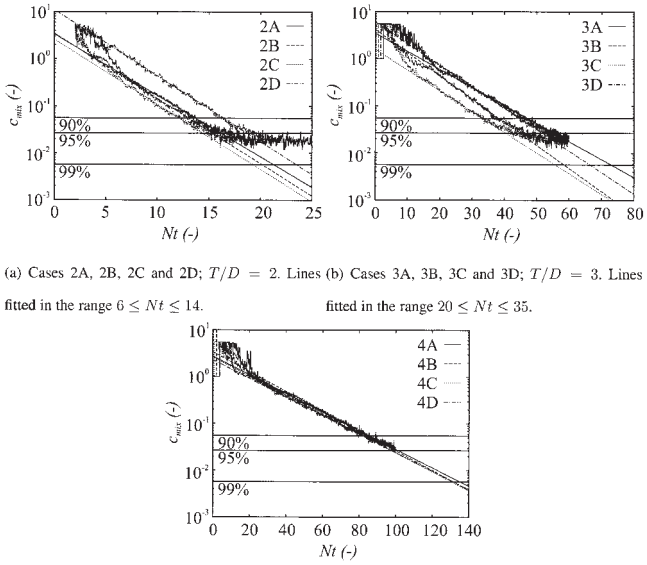

(a) Cases 2A, 2B, 2C and 2D; $T/D = 2$. Lines fitted in the range $6 \leq Nt \leq 14$.

(b) Cases 3A, 3B, 3C and 3D; $T/D = 3$. Lines fitted in the range $20 \leq Nt \leq 35$.

(c) Cases 4A, 4B, 4C and 4D; $T/D = 4$. Lines fitted in the range $40 \leq Nt \leq 80$.

Figure 6. The coefficient of mixing as a function of the dimensionless time.

The horizontal lines labeled 90%, 95% and 99% represent the corresponding concentration percentage.

stabilizes at the value of approximately 0.02. According to Eq. 10, this value corresponds with the 96%–97% concentration, which means that concentration fluctuations of 3%–4% remain. This is clearly unphysical, and these fluctuations are attributed to the numerics.

Table 2 lists the value of the 90%, 95% and 99% mixing times, respectively for all cases. These mixing times are evaluated by intersection of the fitted straight lines (implying exponential decay), and the horizontal lines corresponding to the 90%, 95% and 99% concentration, respectively (see Figure 6). For case 3A, which is the mixing case studied by Distelhoff et al. (1997), it experimentally took 57 impeller revolutions to reach the 99% concentration. The simulation of case 3A predicts that about 47, 55 and 73 impeller revolutions that are needed to obtain the 90%, 95% and 99% concentrations, respectively. The spread of the mixing times with respect to the injection points for the cases 3 (that have $T/D = 3$) is relatively large compared to the $T/D = 2$ and $T/D = 4$ cases. The 99% mixing time for the other three injection positions lie close to the 99% mixing time reported by Distelhoff et al. (1997).

The mixing time in a stirred-tank geometry reported by Yeoh et al. (2005) resembles the 95% mixing time, and equals roughly 33 impeller revolutions. Our results show significantly higher mixing times. While case 3A is most similar to the case studied by Yeoh et al. (2005) (injection position at $r/T = 0.17$ instead of 0.25), the deviation in the mixing time is the largest of all cases (55 vs. 33 revolutions). This deviation can be understood by the fact that in the simulation of Yeoh et al. (2005) the tracer is injected at an injection speed of 15.9 m/s (that is, $1.4 v_{tip}$), whereas in our work the tracer is injected isokinetically. An injection speed introduces jet mixing effects, the passive tracer reaches the impeller region at an earlier time and the mixing time is reduced. As mentioned earlier, the experimental injection conditions are not documented.

Ruszkowski (1994) mixing time correlation

Based on spatial concentration variance measurements Ruszkowski (1994) proposed the following mixing time correlation for Rushton turbine stirred tanks

$$N\theta_m = 5.3 Po^{-1/3} \left(\frac{T}{D}\right)^2 = 3.21 \left(\frac{T}{D}\right)^2 \tag{11}$$

Equation 11 has been criticized for underestimating mixing times by Ruszkowski (1994). Equation 11 is based on a mixing index defined as

$$I_M = 1 - \sqrt{\frac{1}{8} \sum_{i=4n}^{4n+7} \left(\frac{c_{i,rms} - c_\infty}{c_\infty}\right)^2} \tag{12}$$

where n is a time index, c_∞ is the final concentration and $c_{i,rms}$ is defined by

$$c_{i,rms} = \sqrt{\left(\frac{1}{N} \sum_{j=1}^{M} c_{i,j}^2\right)} \tag{13}$$

where M is the number of monitoring points and $c_{i,j}$ is the concentration at a monitoring point j at time $t = i\Delta t$, with Δt the sample time in the experiment. The mixing index expresses the root mean square concentration fluctuation as a fraction of the mean concentration in the tank after addition of the tracer. I_M can vary from $-\infty$ for an "infinitely unmixed" system to 1.0 for a perfectly mixed system. The mixing index is calculated for one section with eight points, the section is moved four data points along the time history and recalculated, and so on. The mixing time was defined as the time for I_M to reach 0.95.

Figure 7a shows the simulated time trace of $1 - I_M$ for the cases 3A, 3B, 3C and 3D. The value of $I_M = 0.95$ is represented by a dashed line. All four cases show that the mixing time equals approximately 29.5 impeller revolutions. Increasing the width of the time window to a blade passage period (Figure 7b) results in less fluctuations of I_M, but it has only a marginal influence on the path of the curves, and, consequently, the mixing time. Despite the mixing vessel geometry of Ruszkowski (1994) was a bit different compared to our system (for example, dished bottom instead of a flat bottom,

Table 2. The Mixing Times for the 90%, 95% and 99% Concentrations, Respectively

Case	$N\theta_{m,90\%}$	$N\theta_{m,95\%}$	$N\theta_{m,99\%}$
2A	13.6	16.0	21.3
2B	13.0	15.1	20.2
2C	12.1	14.2	19.3
2D	16.4	18.5	23.5
3A	46.8	54.7	73.0
3B	38.1	44.2	58.5
3C	33.0	39.8	55.7
3D	44.5	51.1	66.5
4A	85.0	100.2	135.4
4B	84.5	98.7	131.9
4C	81.8	96.5	130.8
4D	81.4	96.6	131.9

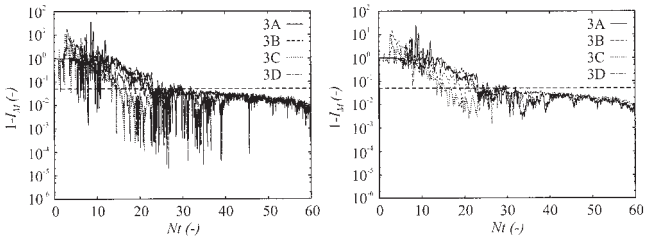

Figure 7. The value of $1 - I_M$ as a function of time for the $T/D = 3$ cases.

The dashed line represents $I_M = 0.95$.

baffle diameter $T/12$ instead of $T/10$), the mixing time predicted by our simulations compares very well with the value of 31 impeller revolutions reported by Ruszkowski (1994).

The mixing time based on $I_M = 0.95$ for the cases 3A, 3B, 3C and 3D equal 32, 30, 24 and 32 impeller revolutions, respectively. With the help of Figure 6b, these mixing times correspond with a coefficient of mixing ranging between 0.12 and 0.22. Translating this in a concentration % via Eq. 10 yields approximately 70%, indeed much lower than the more commonly accepted 95 or 99%.

Performance immersed boundary technique, mass conservation

In this section we check the performance of the ghost cell technique which imposes a zero-normal-gradient at walls that are off-grid (see the section "Ghost cell technique for scalar boundary conditions"). The position of the zero-gradient constraint has been reconstructed with the ghost cell values and two estimated scalar values in the concentration field (that is, similar to the routine described in Section "Ghost cell technique for scalar boundary conditions").

Figure 8a shows a snapshot of the concentration field at $z/T = 0.33$ (that is, disk height) after 15 impeller revolutions. The reconstructed zero-gradient positions are represented by (overlapped) dots. Figure 8b shows an enlarged view of the impeller region. The dots are clearly identified. The lines represent the walls of the impeller geometry. The dots and the lines overlap, which means that the zero-gradient boundary constraint coincides with the geometry walls, as should be expected. The same conclusion is drawn based on Figure 8c that shows an enlarged view near the baffle.

The ghost cell technique does not automatically conserve scalar mass. Therefore, the total mass in the system has been continuously monitored to check the mass conservation constraint. The total mass, M, is calculated as follows

$$M = \sum_{i=1}^{V_{tot}} c_i \Delta V_i \tag{14}$$

where V_{tot} is the amount of control volumes in the flow domain. The total mass normalized with $M_{0.5}$ (the total mass after half an impeller revolution, that is, after stopping the injection) as a function of the dimensionless time for the cases with the $T/D = 3$ impeller is shown in Figure 9a. The time traces of the total mass show (after a startup period) a more-

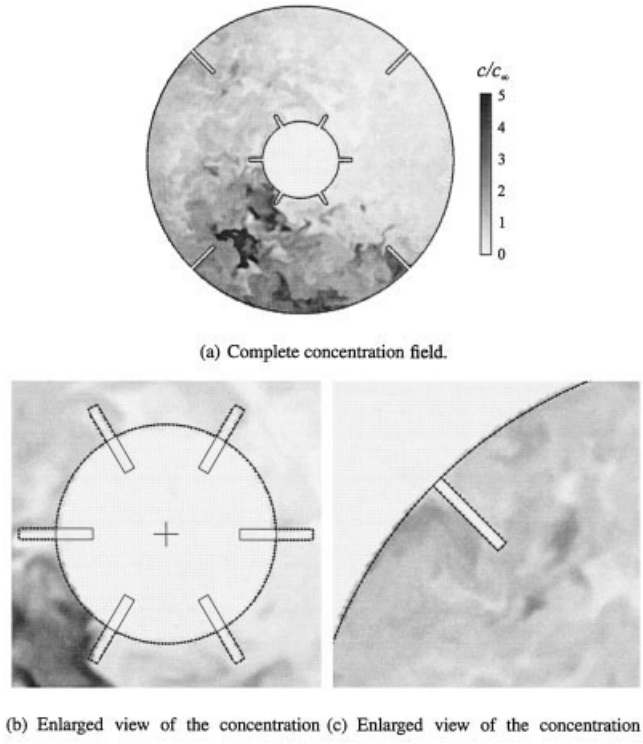

(a) Complete concentration field.

(b) Enlarged view of the concentration field near the impeller.

(c) Enlarged view of the concentration field near the upper left baffle in (a).

Figure 8. Performance immersed boundary technique.

Snapshot of the concentration in a horizontal plane at $z/T = 0.33$ (that is, disk height) and $Nt = 15$. The dots represent the reconstructed position of the zero-gradient boundary condition, the lines represent the walls of the geometry.

or-less linear increase of the total mass. At the end of the simulations, the total mass has increased by 5%–8%.

The mass increase is related to the ghost cell technique for representing offgrid scalar boundary conditions. Simulations with boundary conditions aligned with the grid (such as lid-driven cavity flow, and turbulent planar channel flow) do not suffer from it. Also it is not a result of the lattice-Boltzmann scheme for solving the fluid flow.

The slope of the mass increase depends on the impeller size as can be seen in Figure 9b. An increase of impeller size results in a steeper slope of the mass as a function of time. This observation implies that mass conservation at the impeller

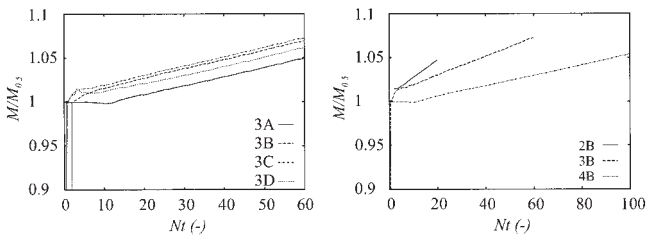

(a) Cases 3A, 3B, 3C and 3D

(b) Cases 2B, 3B and 4B

Figure 9. The dimensionless total mass as a function of time.

$M_{0.5}$ is the total mass after half an impeller revolution (that is, after the addition of the full amount of tracer).

blades is a problem; larger blades result in a larger mass increase.

We strongly believe that the blade edges and/or motion of the boundaries (revolving impeller) play an essential role in mass conservation violation. The motion of boundaries implies that ghost cells turn into active cells and vice versa. If the former happens, the new active cell concentration is taken equal to the ghost cell concentration. This may not be the best choice since the ghost cell concentration has no physical basis (other than maintaining the zero-gradient boundary condition). If an active cell turns into a ghost cell, mass is abruptly taken out of the system without being compensated for exactly at the other side of the impeller.

Near the blade edges, the ghost cell concentrations are involved in two separate zero-gradient boundary conditions, whereas only one concentration per ghost cell is allowed. This also could be a source of error that contributes to the gradual mass increase.

That the blade (and baffle) edges are a problem in conserving the total mass is observed in the time traces shown in Figure 9a. The mass increase of case 3D starts in the early stage of the mixing process, because of the vicinity of a baffle. In case 3C the injection point is in the impeller stream, where the concentration is strongly advected radially outward toward the baffles. In case 3B the injection point is $0.1T$ above the impeller, and the mass increase starts at roughly $Nt = 2$. In case 3A, the mass injection point is at the top of the tank, and it takes some time for the concentration being advected toward the impeller region. As a result, the mass increase is expected at a later moment in time (that is, $Nt = 10$) compared to the other cases (see for example, the instantaneous concentration fields in Figure 3).

In summary, the ghost cell technique developed positions accurately the zero-gradient constraint at the geometry walls (Figure 8), but the mass conservation constraint is not satisfied (Figure 9). The mass increase is significant (5%–8%), and in future research the current technique needs to be improved.

Conclusions

In this article, we have coupled a lattice-Boltzmann based large-eddy simulation of the flow in a mixing tank to a passive scalar transport solver based on the finite volume method. Specific care was taken to suppress numerical diffusion of the scalar, and to accurately represent the zero-gradient scalar boundary conditions at the (offgrid and partly moving) walls.

We have related the mixing time to a coefficient of mixing, that provides a spatial concentration variance over the entire tank. Simulated time traces of the coefficient of mixing revealed (after a startup phase) an exponential decay, similar to experimental findings (Ruszkowski, 1994). At the end of the calculations, the coefficient of mixing stabilized at about 0.02. This is unphysical, and this effect is attributed to the numerics. The exponential decay has been extrapolated toward zero through a fitting procedure. The mixing times were defined by the intersection of the fitted lines and the calibrated values of the 90%, 95%, and 99% concentration criterions, respectively.

The mixing time is significantly influenced by the impeller size. The simulated mixing times agree within 30% with experimentally obtained values. Our work has revealed that the Ruszkowski (1994) mixing time correlation corresponds to a 70% concentration criterion.

The position of the tracer injection point does not significantly affect the mixing time. While a spread of the simulated mixing time was observed in the $T/D = 3$ cases, it was found to be clearly less significant in the $T/D = 2$, and $T/D = 4$ cases. The predicted 99% mixing time in the case similar to the experiment of Distelhoff et al. (1997) overestimates the experimentally obtained mixing time with some 26%.

Our novel immersed boundary technique does not guarantee mass conservation. The average mass increase per impeller revolution depends on the impeller size being 0.25%, 0.125%, and 0.05% for the impeller sizes $T/D = 2$, $T/D = 3$ and $T/D = 4$, respectively. The unphysical mass increase is attributed to the motion of the boundaries (impeller), and to mass leakage at the edges (of the impeller and baffles).

The violation of mass conservation clearly is a problem, and needs to be repaired in future work. Our present efforts towards mass conservation involve the possibility of dual or triple concentrations per ghost cell (note that ghost cell concentrations do not have physical meaning, they only serve the numerics) for determining fluxes in different directions.

In our view, however, mass conservation violation does not interfere with the main messages of the article which are: (1) the mixing of a passive scalar in the very complex turbulent flow in an agitated tank is very realistically modeled, and the structures observed agree with those observed in for example, planar laser-induced fluorescence experiments, and (2) the simulated time traces agree in terms of fluctuation levels and time scales with the experimental time traces reported by Distelhoff et al. (1997). As a result, we do not think that the spurious concentration fluctuations that become apparent in a later stage of the mixing process and the violation of mass conservation are related. Furthermore, we preferred the uncertainties when extrapolating to the 99% mixing time introduced by the slight wiggles in the solution of the concentration over the excessive numerical diffusion introduced by a simple first-order upwind scheme.

Notation

A = surface area, m^2
c = concentration, $kg \cdot m^{-3}$
$c_{i,rms}$ = the rms concentration at time, $i\Delta t$
c_{mix} = coefficient of mixing
$\bar{c}$ = spatial average of the concentration, $kg \cdot m^{-3}$
c_∞ = final concentration, $kg \cdot m^{-3}$
$c_{\%}$ = concentration %
D = impeller diameter, m
F_C = convective prefactor in Eq. 2, $kg \cdot s^{-1}$
F_D = diffusive prefactor in Eq. 2, $kg \cdot s^{-1}$
H = height of the tank, m
I_M = mixing index defined by Ruszkowski (1994)
K = number of monitoring points
n = time index
N = impeller speed, s^{-1}
M = total mass, kg
$M_{0.5}$ = injected mass after half an impeller revolution, kg
Po = power number
r = radial coordinate, m
r = upwind ratio of consecutive gradients
r_p = radius of the feed pipe, m
Re = Reynolds number
S_ϕ = source term in convection-diffusion equation, $kg \cdot m^{-3} \cdot s^{-1}$
Sc_t = turbulent Schmidt number

t = time, s
T = tank diameter, m
u = velocity, $m \cdot s^{-1}$
u_i = velocity component i, $m \cdot s^{-1}$
x_i = coordinate i, m
z = axial coordinate, m

Greek letters

Γ = diffusion coefficient, $m^2 \cdot s^{-1}$
Γ_e = eddy diffusion coefficient, $m^2 \cdot s^{-1}$
Γ_{mol} = molecular diffusion coefficient, $m^2 \cdot s^{-1}$
Δt = time step, s
ΔV = finite volume, m^3
θ = angle, °
θ_m = mixing time, s
ν = kinematic viscosity, $m^2 \cdot s^{-1}$
ν_e = Smagorinsky eddy viscosity, $m^2 \cdot s^{-1}$
ρ = density, $kg \cdot m^{-3}$
ϕ = general scalar variable
Ψ = flux limiter

Literature Cited

Bakker, A., and L. M. Oshinowo, "Modelling of turbulence in stirred vessels using large eddy simulation," *Chemical Engineering Research and Design,* **82**(**A9**), 1169 (2004).

Bouwmans, I., A. Bakker, and H. E. A. Van den Akker, "Blending liquids of different viscosities and densities in stirred vessels," *Chem Engg Res & Design,* **75**(**A8**), 777 (1997).

Bujalski, W., Z. Jaworski, and A. W. Nienow, "CFD study of homogenization with dual Rushton turbines—comparison with experimental results," *Chem Engg Res and Design,* **80,** 97 (2002).

Calhoun, D., and R. J. LeVeque, "A Cartesian grid finite volume methode for the advection-diffusion equation in irregular geometries," *J of Comput Phys,* **157,** 143 (2000).

Chen, S., and G. D. Doolen, "Lattice-Boltzmann method for fluid flows," *Annual Review of Fluid Mechanics,* **30,** 329 (1998).

Derksen, J. J., "Numerical Simulation of Solids Suspension in a Stirred Tank," *AIChE J,* **49,** 2700 (2003).

Derksen, J. J., and H. E. A. Van den Akker, "Large Eddy Simulations on the Flow Driven by a Rushton Turbine," *AIChE J,* **45,** 209 (1999).

Distelhoff, M. F. W., A. J. Marquis, J. H. Nouri, and J. M. Whitelaw, "Scalar Mixing Measurements in Batch Operated Stirred Tanks," *Canadian J of Chem Engg,* **75,** 641 (1997).

Eggels, J. G. M., "Direct and Large Eddy Simulations of Turbulent Fluid Flow using the Lattice-Boltzmann Scheme," *Intl J of Heat and Fluid Flow,* **17,** 307 (1996).

Eggels, J. G. M., and J. A. Somers, "Numerical Simulation of Free Convective Flow using the Lattice-Boltzmann Scheme," *Intl J of Heat and Fluid Flow,* **16,** 357 (1995).

Harten, A., "High Resolution Schemes for Hyperbolic Conservation Laws," *J of Computational Physics,* **49,** 357 (1983).

Hartmann, H., J. J. Derksen, C. Montavon, J. Pearson, I. S. Hamill, and H. E. A. Van den Akker, "Assessment of Large eddy and RANS Stirred Tank Simulations by Means of LDA," *Chem Eng Sci,* **59,** 2419 (2004a).

Hartmann, H., J. J. Derksen, and H. E. A. Van den Akker, "Macro-Instability Uncovered in a Rushton Turbine Stirred Tank," *AIChE J,* **50,** 2383 (2004b).

Holmes, D. B., R. M. Voncken, and J. A. Dekker, "Fluid Flow in Turbine Stirred, Baffled Tanks I: Circulation time," *Chem Engg Sci,* **19,** 201 (1964).

Hoogendoorn, C. J., and A. P. Den Hartog, "Model Studies on Mixers in Viscous Flow Regions," *Chem Engg Sci,* **22,** 1689 (1967).

Houcine, I., H. Vivier, R. David, and J. Villermaux, "Comparison of Mixing Action of Several Stirrers by Laser Sheet Visualization and Image Processing," In: *IChemE Symposium Series 136,* 97–104 (1994).

Jaworski, Z., W. Bujalski, N. Otomo, and A. W. Nienow, "CFD Study of Homogenization with Dual Rushton Turbines—Comparison with Experimental Results. Part I: Initial Studies," *Chem Engg Res and Design,* **78,** 327 (2000).

Kramers, H., G. M. Baars, and W. H. Knoll, "A comparative study on the rate of mixing in stirred tanks," *Chem Engg Sci,* **2,** 35 (1953).

Lee, K. C., *An experimental investigation of the trailing vortex structure and mixing characteristics of mixing vessels,* Ph.D. Thesis, King's College London, University of London (1995).

Leonard, B. P., "A Stable and Accurate Convective Modelling Procedure Based on Quadratic Upstream Interpolation," *Comp Methods in Applied Mech and Eng,* **19,** 59 (1979).

Moo-Young, M., K. Tichar, and F. A. L. Takahashi, "The blending efficiencies of some impellersin batch mixing," *AIChE J,* **18,** 178 (1972).

Osman, J. J., and J. Varley, "The Use of Computational Fluid Dynamics (CFD) to Estimate Mixing Times in a Stirred Tank." In: *IChemE Symposium Series,* 146, 15–22 (1999).

Patankar, S. V., *Numerical Heat Transfer and Fluid Flow,* Hemisphere Publ. Corp. (1980).

Prochazka, J., and J. Landau, "Studies on mixing XII. homogenation of miscible liquids in the turbulent region," *Coll Czech Chem Commun,* **26,** 2961 (1961).

Roe, P. L., "Approximate Riemann-solvers, parameter vectors and difference schemes," *J of Computational Physics,* **43,** 357 (1981).

Rushton, J. H., E. W. Costich, and H. J. Everett, "Power characteristics of mixing impeller I and II." *Chem Eng Progr,* **46,** 395 (1950).

Ruszkowski, S., "A Rational Method for Measuring Blending Performance, and Comparison of Different Impeller Types," In: *Proceedings of the 8th European conference on mixing,* September 21st–23rd, Cambridge, U.K. (1994).

Sano, Y., and H. Usui, "Interrelations Among Mixing Time, Power Number and Discharge Flow Rate Number in Baffled Mixing Vessels," *J of Chem Eng J,* 47–52 (1985).

Schäfer, M., M. Yianneskis, P. Wächter, and F. Durst, "Trailing Vortices Around a 45° Pitched-Blade Impeller," *AIChE J,* **44,** 1233 (1998).

Shiue, S. W., and C. W. Wong, "Studies on Homogenization Efficiency of Various Agitators in Liquid Blending," *CJ of Chem Engg,* **62,** 602 (1984).

Smagorinsky, J., "General Circulation Experiments with the Primitive Equations: 1. The Basic Experiment," *Monthly Weather Review,* **91,** 99 (1963).

Somers, J. A., "Direct Simulations of Fluid Flow with Cellular Automata and the Lattice-Boltzmann Equation," *Applied Scientific Research,* **51,** 127 (1993).

Tucker, P. G., and Z. Pan, "A Cartesian Cut Cell Method for Incompressible Viscous Flow," *Applied Math Modelling,* **24,** 591 (1999).

Wang, Y., and K. Hutter, "Comparisons of Numerical Methods with Respect to Convectively Dominated Flows," *Intl Journal for Numerical Methods in Fluids,* **37,** 721 (2001).

Yeoh, S. L., G. Papadakis, K. C. Lee, and M. Yianneskis, "Large Eddy Simulation of Turbulent Flow in a Rushton Impeller Stirred Reactor with Sliding-Deforming Mesh Methodology," *Chem Eng and Technol,* **27,** 257 (2004).

Yeoh, S. L., G. Papadakis, and M. Yianneskis, "Determination of Mixing Time and Degree of Homogenity in Stirred Vessels with Large Eddy Simulation," *Chem Eng Sci,* **60,** 2293 (2005).

Yianneskis, M., Z. Popiolek, and J. H. Whitelaw, "An Experimental Study of the Steady and Un-Steady Flow Characteristics of Stirred Reactors," *J of Fluid Mechanics,* **175,** 537 (1987).

Appendix

Consider a set of K statistically independent, dimensionless concentrations ranging between 0.99 and 1.01. The dimensionless concentrations are obtained at the monitoring points. With these numbers, a coefficient of mixing can be calculated. If we repeat this experiment L times (that is, inclusion of time as a variable), we obtain a distribution function of the coefficient of mixing for the 99% concentration. The experiment is repeated for other concentration percentages.

Figure A1a shows a calibration graph of the coefficient of mixing vs. the concentration %. The total number of monitoring points (K) equals 32, and the number of repetition (L) was set at 10^5, which resembles a time interval comparable to the length of the simulated time series. The graph shows that with

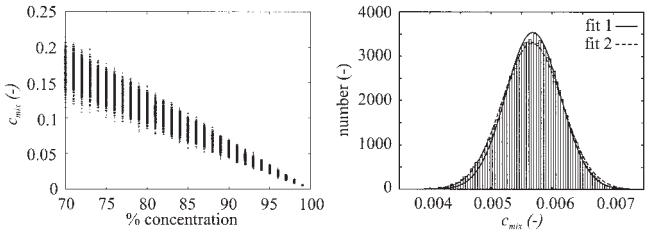

Figure A1. Calibration graph (a) of coefficient of mixing vs. concentration %.

The histogram of the coefficient of mixing at 99% concentration is shown in (b), together with two Gaussian fits.

increasing concentration %, the average coefficient of mixing decreases, and the distribution becomes narrower as expected.

Figure 10b shows the histogram of the coefficient of mixing for the 99% concentration. The distribution function is nearly Gaussian, as shown by the two Gaussian fits. Gaussian fit 1 is fitted in the range 0.0045–0.006 and fit 2 in the range 0.005–0.0065. The average coefficient of mixing that can be linked to the 99% concentration equals 0.00566. For the 95% and 90% concentrations, the average coefficient of mixing equals 0.0283 and 0.0566, respectively. A linear fit with a negative slope through the data shown in Figure 10a results in the relationship given by Eq. 10.

Manuscript received May 22, 2006, and final revision received Aug. 9, 2006.